ADVANCED MATERIALS
www.advmat.de

Exchange-Biased Quantum Anomalous Hall Effect

*Peng Zhang, Purnima P. Balakrishnan, Christopher Eckberg, Peng Deng, Tomohiro Nozaki, Su Kong Chong, Patrick Quarterman, Megan E. Holtz, Brian B. Maranville, Gang Qiu, Lei Pan, Eve Emmanouilidou, Ni Ni, Masashi Sahashi, Alexander Grutter, and Kang L. Wang**

The quantum anomalous Hall (QAH) effect is characterized by a dissipationless chiral edge state with a quantized Hall resistance at zero magnetic field. Manipulating the QAH state is of great importance in both the understanding of topological quantum physics and the implementation of dissipationless electronics. Here, the QAH effect is realized in the magnetic topological insulator Cr-doped $(Bi,Sb)_2Te_3$ (CBST) grown on an uncompensated antiferromagnetic insulator Al-doped Cr_2O_3. Through polarized neutron reflectometry (PNR), a strong exchange coupling is found between CBST and Al-Cr_2O_3 surface spins fixing interfacial magnetic moments perpendicular to the film plane. The interfacial coupling results in an exchange-biased QAH effect. This study further demonstrates that the magnitude and sign of the exchange bias can be effectively controlled using a field training process to set the magnetization of the Al-Cr_2O_3 layer. It demonstrates the use of the exchange bias effect to effectively manipulate the QAH state, opening new possibilities in QAH-based spintronics.

1. Introduction

The quantum anomalous Hall (QAH) effect arises due to the combination of topologically nontrivial band structures and ferromagnetism-induced time-reversal symmetry breaking. Characterized by a quantized Hall resistance with vanishing longitudinal resistance at zero magnetic field, it was first observed experimentally in magnetically doped topological insulator (MTI) thin films, Cr- and V- doped $(Bi,Sb)_2Te_3$,[1–6] and more recently observed in the intrinsic magnetic topological material $MnBi_2Te_4$,[7] twisted bilayer graphene,[8] and $MoTe_2/WSe_2$ Moiré heterostructures.[9] In addition to developing new MTIs, extensive efforts have been devoted to proximity-coupling a topological insulator (TI) or MTI material to other strongly magnetically ordered compounds in order to engineer the time-reversal symmetry breaking in topological surface states. Proximity coupling to more uniform or stronger magnetic materials has, for example, been employed to introduce ferromagnetism into otherwise nonmagnetic TIs[10–19] and to enhance the Curie temperature T_C of MTI films.[20–23] Moreover, the proximity effect through the interface also implements exchange coupling as an additional degree of freedom through which the topological surface states can be manipulated.

While successful epitaxial integration of MTIs with (anti)ferromagnetic ((A)FM) layers[10–27] have provided a route

P. Zhang, C. Eckberg, P. Deng, S. K. Chong, G. Qiu, L. Pan, K. L. Wang
Department of Electrical and Computer Engineering
University of California Los Angeles
Los Angeles, CA 90095, USA
E-mail: wang@ee.ucla.edu

P. P. Balakrishnan, P. Quarterman, B. B. Maranville, A. Grutter
NIST Center for Neutron Research
National Institute of Standards and Technology
Gaithersburg, MD 20899–6102, USA

C. Eckberg
Fibertek Inc.
Herndon, VA 20171, USA

C. Eckberg
US Army Research Laboratory
Adelphi, MD 20783, USA

C. Eckberg
US Army Research Laboratory
Playa Vista, CA 90094, USA

T. Nozaki, M. Sahashi
Department of Electronic Engineering
Tohoku University
Sendai 980-8579, Japan

M. E. Holtz
Material Measurement Laboratory
National Institute of Standards and Technology (NIST)
Gaithersburg, Maryland 20899, USA

E. Emmanouilidou, N. Ni, K. L. Wang
Department of Physics and Astronomy
University of California Los Angeles
Los Angeles, CA 90095, USA

K. L. Wang
Department of Materials Science and Engineering
University of California
Los Angeles, CA 90095, USA

The ORCID identification number(s) for the author(s) of this article can be found under https://doi.org/10.1002/adma.202300391

DOI: 10.1002/adma.202300391

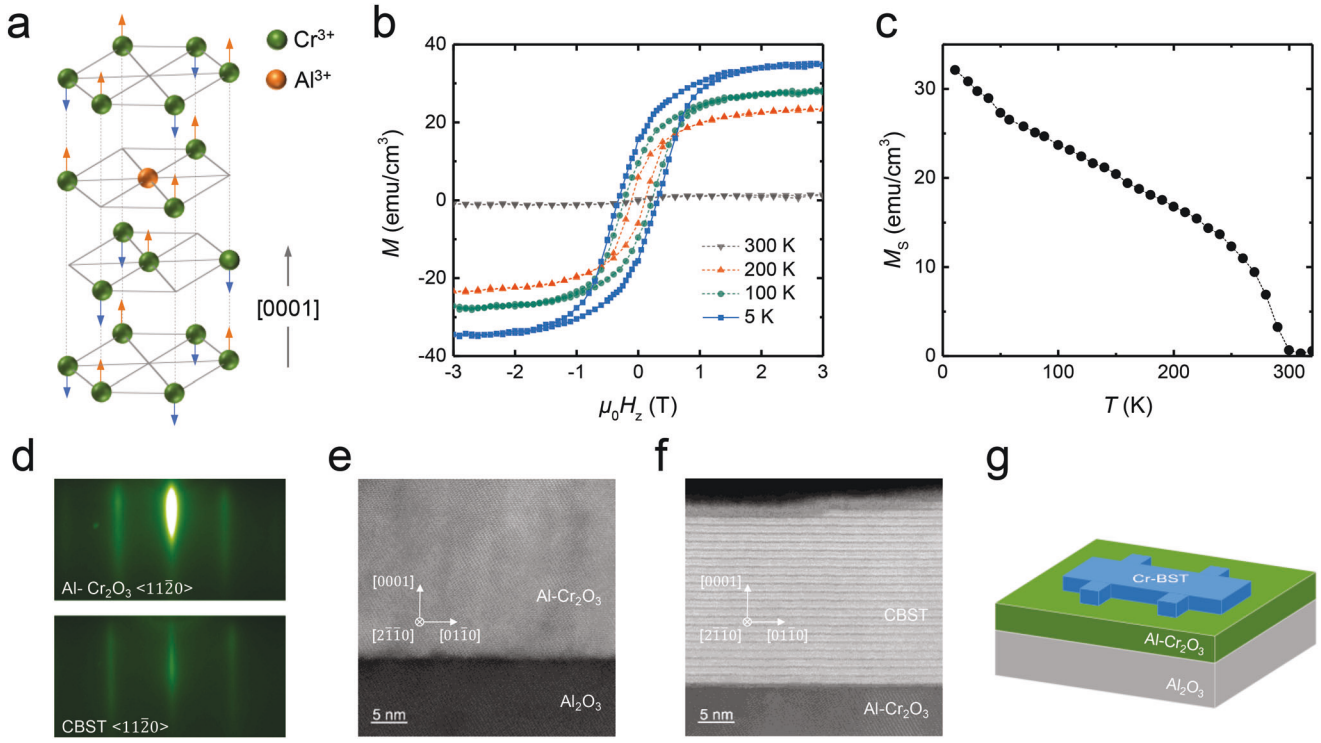

Figure 1. High quality Cr doped BST grown by molecular beam epitaxy on Al-doped Cr_2O_3 (0001). a) Atomic and magnetic structure of Al-doped Cr_2O_3. Oxygen atoms are omitted for simplicity. Al^{3+} substitution of Cr^{3+} change the AFM Cr_2O_3 into a ferrimagnetic-like magnetic structure. b) M-H_z profile of 50 nm Al-Cr_2O_3 substrate showing hysteresis loops below 300 K. A linear, diamagnetic background associated with the Al_2O_3 substrate has been subtracted from all presented curves. c). Temperature dependence of saturated magnetic moment of 50 nm Al-Cr_2O_3 substrate measured with an out-of-plane filed of +2 T. d) RHEED pattern of the Al-Cr_2O_3 substrates and MBE grown CBST on top along <11-20> direction. e) HAADF-STEM of the Al_2O_3/Al-Cr_2O_3 interface. f) HAADF-STEM of the Al-Cr_2O_3/CBST interface. g) Hall-bar structure (1 mm by 0.5 mm) used for transport measurement.

to control magnetic topological states, prior achievements in exchange biasing MTIs have suffered from several critical limitations. Most notably, magnetic exchange bias in MTI layers has historically been achieved only at the expense of quantized behavior, and to date, simultaneous observation of quantized transport and magnetic exchange bias in MTI/AFM bilayers has remained elusive. Challenges in manipulating the AFM Néel vector directly have imparted further constraints on prior MTI exchange bias efforts, resulting in systems vulnerable to exchange bias aging and multi-domain formation. It has been speculated that the difficulty in realizing edge state quantization at the same time as exchange bias may be related to inhomogeneities in the magnetic configuration of the uncompensated spins at the AFM surface.[24] Such inhomogeneities have long been suspected to play a critical role in preventing high-temperature quantization in doped MTI films due to the resulting exchange gap modulation,[28–30] and exchange bias inherently relies on relatively dilute defect states to act as pinned spins.

2. Results and Discussion

2.1. MTI on Uncompensated AFM

These homogeneity issues may be resolved through the introduction of a small net moment. Cr_2O_3 is an antiferromagnetic insulator with a Néel temperature T_N near or above room temperature and is a suitable substrate for the growth of high-quality MTI.[24,26] While Cr_2O_3 imparts exchange bias in an adjacent MTI layer, exchange bias and quantized edge transport have never been simultaneously observed in this system. On its own, Cr_2O_3 is of interest as a magnetoelectric material with potential applications in electrical control of either AFM domains or adjacent ferromagnetic (FM) layers through exchange coupling.[31–34] While this makes Cr_2O_3 promising for low-energy spintronic applications, the single domain state necessary for practical applications is challenging to achieve in this AFM material. Prior works have achieved a single-domain state by reducing film thickness to decrease T_N below the T_C of the MTI such that the orientation of spins can be controlled deterministically.[26] The introduction of nonmagnetic Al dopants into the Cr_2O_3 thin film during the growth yields a ferrimagnetic-like moment also known as a parasitic magnetization. This emergent magnetization has been attributed to the preferential occupation of Al on one of the two Cr sublattices.[35,36] As illustrated in **Figure 1**a, the Cr spins in pure Cr_2O_3 align parallel or antiparallel to [0001] forming a Néel vector along the *c*-axis, while the introduction of Al dopants breaks the symmetry of the two AFM sublattices and imparts a small net magnetization.

Here, we finally demonstrate the simultaneous observation of both exchange bias and the QAH effect in MTI films epitaxially deposited on Al-doped Cr_2O_3. Through detailed neutron reflectivity and electrical transport characterization, we demonstrate

high quality transport quantization in the MTI layer along with a robust magnetic coupling between the AFM and MTI at the material interface. The latter feature results in a strong magnetic exchange bias in the MTI layer observed to persist over a wide range of temperature both within and outside of the quantized regime. Meanwhile, in contrast to a pure AFM state, the parasitic magnetization in the Al-Cr_2O_3 layer is shown to couple directly with a magnetic field. Taking advantage of this engineered field sensitivity, we demonstrate the capability to systematically tune the AFM magnetic order, and through it the magnet exchange bias in the MTI, using an external magnetic field. Beyond enabling the reliable realization of a single domain state in the AFM layer, magnetic controllability eliminates the impractical requirement of thermal training the AFM when writing the exchange bias in the bilayer system. These concurrent advancements demonstrate heretofore unrealized capabilities in MTI exchange bias engineering, and further establish the viability of a system that may in the future yield all-electrical control of quantum Hall edge states.

The 50 nm thick 3.7% Al-doped Cr_2O_3 was deposited on α-Al_2O_3 (0001) substrates by magnetron sputtering, and its magnetic properties were characterized using a superconducting quantum interference device (SQUID) magnetometer. Figure 1b shows the out-of-plane magnetization profile of the Al-doped Cr_2O_3 measured at multiple temperatures. Clear hysteresis loops were observed, consistent with the expected ferrimagnetic-like dopant-induced parasitic magnetization, which combined with the observation of hysteresis loops under the in-plane field with a lower saturation magnetization (Figure S1, Supporting Information), indicates a perpendicular magnetic anisotropy (PMA). The temperature evolution of the saturated magnetization in Figure 1c indicates a critical temperature near 300 K, which is consistent with the Néel temperature (T_N) of 307 K[34] in pristine Cr_2O_3.

To fabricate the Al-Cr_2O_3/MTI bilayers presented in this study, Cr doped $(Bi,Sb)_2Te_3$ (CBST) layers were consequently grown on 50 nm thick Al-doped Cr_2O_3 using molecular beam epitaxy (MBE). CBST layers were grown with a thickness of 6 quintuple layer (QL) for transport studies, while thicker films (20 QL) were prepared for high-angle annular dark-field scanning transmission electron microscopy (HAADF-STEM) characterization and polarized neutron reflectometry (PNR) studies. Both the sputtered Al-Cr_2O_3 and MBE grown CBST showed good single-crystalline quality, as indicated by the streaky reflection high-energy electron diffraction (RHEED) patterns both before and after the epitaxy of CBST (Figure 1d). An atomically sharp interface between Al_2O_3 and Al-Cr_2O_3, as well as the sharp interface to the CBST layer can be seen from the HAADF-STEM in Figure 1e,f, respectively.

2.2. Interfacial Coupling

To probe the interfacial coupling between the Al-doped Cr_2O_3 and CBST, we performed PNR measurements on a 20 QL CBST film grown on 50 nm Al-doped Cr_2O_3. PNR gives a measure of the depth-dependent magnetization of these bilayers. Specular reflectometry ($\vec{Q}$ perpendicular to the surface) is sensitive to in-plane moments only, so measurements were performed with an in-plane applied field, at a base temperature of 6 K. The summed spin-dependent reflectivity ($R^{++} + R^{--}$) and spin-dependent splitting ($R^{++} - R^{--}$) extracted from these measurements are plotted on the Fresnel scale in **Figure 2**a–d along with the best-fit nuclear and magnetic profiles shown in Figure 2e. PNR indicates a large-scale, high-quality heterostructure, yielding nuclear scattering length densities (SLDs) within 1% of the theoretical bulk values for each material and a smooth functional interface between Al-doped Cr_2O_3 and CBST of the same roughness as the substrate. There is no evidence for a transitional growth region between these layers, as has been observed in some recent studies of oxide/topological insulator heterostructures,[37,38] so any magnetic differences at this interface can be attributed to exchange coupling rather than chemical or structural differences.

As has been previously reported in related Cr_2O_3/CBST structures, the interface of this system is magnetically complex. Past work[24,26] indicated antiparallel alignment of the CBST and Cr_2O_3 spins along with strong out-of-plane pinning of the CBST magnetization at the interface. This pinning was attributed to exchange coupling with the unusual surface reconstruction of Cr_2O_3 that leads to spins fixed along the [0001] direction. In this context, we note that the best-fit model indicates a region of zero in-plane magnetization at the interface between the CBST and Al-Cr_2O_3 at all measured fields. As the in-plane field decreases, the thickness of this region across both layers grows, from 2.073(15) nm at 3 T to 2.857(26) nm at 250 mT and finally to 4.079(23) nm at 110 mT. While the absence of any in-plane magnetization in this region could indicate the presence of a magnetic dead layer, its variable thickness is more consistent with reconstructed surface spins with giant magnetic anisotropy. Given that magnetically dead layers are rarely observed in CBST films, and a robust and repeatable exchange biasing effect in these films is observed, we conclude that a conventional dead layer at the interface is unlikely. Rather, we propose that a strong antiparallel exchange coupling between the CBST and Al-Cr_2O_3 surface spins pins the interfacial magnetization along the film normal, where PNR is insensitive.

Further supporting this picture, the best model is one in which the magnetic moments within the CBST layer gradually cant from an out-of-plane orientation at the interface toward the in-plane direction at the top surface of the film. A schematic of the moment orientation is shown in Figure 2f. The moments in the CBST layer, up to a maximum of 30.4(9) emu cc^{-1} (1 emu cc^{-1} = 1 kA m^{-1} = 2.91 × 10^{-7} nm^{-2}) in-plane at 3 T, have a larger in-plane component canting over longer length scales as the field decreases, indicating strong exchange coupling between Cr moments within the CBST; at 110 mT, the magnetization rotates from 9.7(8) emu cc^{-1} in-plane to 12.8(8) emu cc^{-1} in-plane. However, this gradual moment canting is not present in the Al-Cr_2O_3 layer, which exhibits a uniform increase in magnetization with increasing field. This matches the magnetometry observation that Al-Cr_2O_3 has stronger perpendicular magnetic anisotropy than CBST. Further, the maximum in-plane magnetization at 7 K and 3 T in-plane of 19.2(4) emu cc^{-1} within the Al-Cr_2O_3 extracted from the PNR result matches the saturation magnetization of the in-plane hysteresis behavior measured using SQUID (22 emu cc^{-1}, Figure S1, Supporting Information), which is suppressed from the out-of-plane saturation magnetization of 35 emu cc (Figure 1b). We conclude, therefore, that some fraction of the Al-Cr_2O_3 spins remain pinned along the

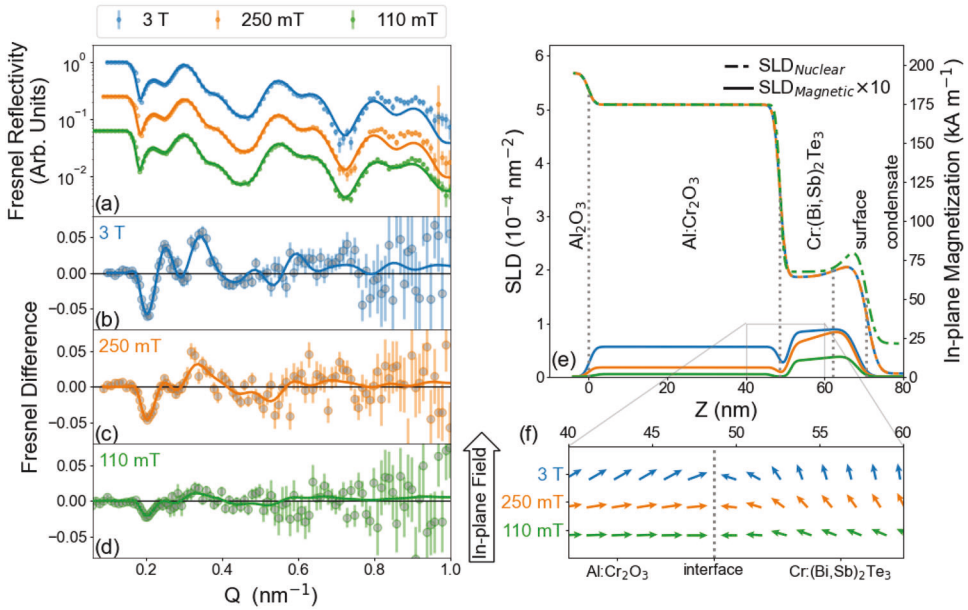

Figure 2. Interfacial coupling between Al-Cr_2O_3 and CBST layers probed by PNR. a) Fresnel reflectivity ($\frac{R^{++}+R^{--}}{R(Al_2O_3)}$) scaled to be offset and b–d) difference ($\frac{R^{++}-R^{--}}{R(Al_2O_3)}$) for an Al-$Cr_2O_3$/CBST bilayer measured by polarized neutron reflectometry with applied in-plane magnetic fields of b) 3 T (blue), c) 250 mT (orange), and d) 110 mT (green). Solid lines show the best fits, which are generated by e) nuclear and in-plane magnetic depth-profile models at each field. Magnetic scattering length density (SLD) has been scaled by a factor of 10 with respect to the SLD axis for clarity but corresponds to the magnetization as plotted (2.91×10^{-7} nm^{-2} = 1 kA m^{-1} = 1 emu cm^{-3}). Differences in the nuclear SLD profiles at the surface between subsequent measurements are likely due to sample aging, as discussed in Figure S3 (Supporting Information). f) Possible orientation and relative magnitude of the net magnetization near the interface, deduced from e) the in-plane magnetization, and magnetometry results. This schematic assumes that the Al-Cr_2O_3 sublattices rotate together and does not illustrate the effect of domains.

film normal at all fields. Comparisons with alternate models, without these features, can be found in Figure S2 (Supporting Information).

2.3. Exchange–Biased QAH Effect

Having measured the vertical magnetization profile in Al-Cr_2O_3/CBST bilayers, we carried out transport measurements to show the exchange-biased QAH effect in these heterostructures. The films were patterned into Hall-bar devices with a geometry of 1 by 0.5 mm, as previously shown in Figure 1g, using a hard mask and dry etching method. The samples were cooled down to 50 mK under a +1 T perpendicular magnetic field. **Figure 3**a shows a vanishing longitudinal resistance ρ_{xx} and quantized Hall resistance ρ_{xy} at cryogenic temperature, confirming these films do indeed display the typical signatures of the QAH effect. For further confirmation, conductivity tensor components were computed using the relations $\sigma_{xx} = \rho_{xx}/(\rho_{xx}^2 + \rho_{xy}^2)$ and $\sigma_{xy} = \rho_{xy}/(\rho_{xx}^2 + \rho_{xy}^2)$ that also show perfect quantization (Figure 3b). The sample was then subjected to a magnetic field sweep between ± 0.2 T. The field sweep range was larger than the coercivity of CBST but smaller than that of Al-Cr_2O_3, so that the magnetization of the latter remained intact during the sweep. The evolution of σ_{xx} versus σ_{xy} upon the field sweep is shown by the flow diagram in Figure 3c. It shows the transition between the two quantized Chern insulator states with Chern number $c = \pm 1$, $(\sigma_{xy},\sigma_{xx}) = (c, 0)$, and an intermediate trivial insulator state, $(\sigma_{xy},\sigma_{xx}) \rightarrow (0, 0)$, which is observed in QAH insulators with thickness $t \leq 6$ QL due to a competition between the magnetic exchange gap and surface hybridization gap.[3,39,40] The sample was then trained with ± 3 T followed by a field sweep between ± 0.2 T. The magnetic field dependence of ρ_{xx} and ρ_{yx} during the sweep are shown in Figure 3d,e respectively. Remarkably, the sample showed an exchange-biased quantum anomalous Hall effect: the magnetic exchange bias was observed simultaneously with the QAH effect. It is clearly evidenced by a coercivity shift in ρ_{yx} and corresponding peak shift in ρ_{xx} under different Al-Cr_2O_3 magnetization initialization status, with a magnitude of $\approx 2\mu_0 H_{eb} \approx 16$ mT. It is unlikely that this exchange bias is caused by artificial effects such as the remnant field of a superconducting magnet, as discussed in detail in Figures S5–S8 (Supporting Information). A slightly asymmetric behavior of ρ_{xx}, which fully reverses, could be due to different spin texture at the Al-Cr_2O_3 and CBST interface under different field training conditions. This observation showed that the presence of the exchange bias from the Al-Cr_2O_3 layer could effectively manipulate the QAH state in CBST.

In addition, we would like to emphasize that the exchange-biased QAH effect can be controlled by a novel field-training (FT) approach, rather than requiring the traditional field cooling (FC) method. Field cooling is usually used to align the Néel vector of AFM materials, by applying a magnetic field and cooling through the Néel temperature T_N. In Al-Cr_2O_3, it is the introduction of Al dopants that breaks the symmetry of the two AFM sublattices and produces a nonzero net magnetization as indicated in the SQUID

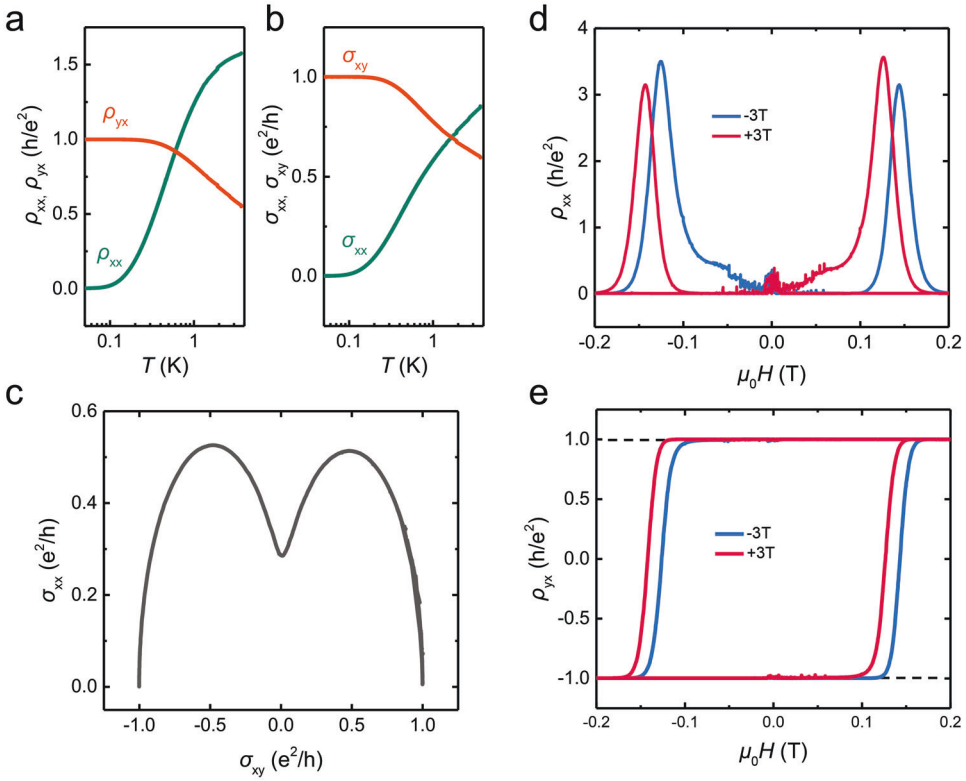

Figure 3. Observation of exchange-biased quantum anomalous Hall effect in Al-Cr_2O_3/CBST heterostructure. a) Temperature dependences of longitudinal resistivity ρ_{xx} and Hall resistivity ρ_{yx} under 1 T field, where ρ_{xx} vanishes and ρ_{yx} approaches the quantized value of h/e^2 with decreasing temperature. b) Temperature dependences of σ_{xx} and σ_{xy} converted from ρ_{xx} and ρ_{yx}. c) Evolution of the σ_{xx} versus σ_{xy} when scanning the magnetic field at 50 mK. d,e) Magnetic field dependences of ρ_{xx} and ρ_{yx} after training the sample using −3 T and +3 T to polarize the Al-Cr_2O_3 magnetization. The magnetic field was swept between ±0.2 T and the data was taken at 50 mK.

and PNR experiments. While an external magnetic field cannot couple to a perfectly compensated AFM order parameter, it can be used to switch the ferrimagnetic-like magnetic order in Al-Cr_2O_3. The use of Al-Cr_2O_3 thus has a significant advantage over its undoped counterpart Cr_2O_3 as the sign of any exchange bias may be changed through the application of an external magnetic field alone, without requiring the system be raised above its Néel temperature. To demonstrate this advantage, we performed measurements from both field cooling and field training initialization methods. In field cooling, the sample was subjected to ±3 T fields while cooling down from above T_N = 330 to 2 K. In field training, the sample was cooled down to 2 K without applying field and then was subjected to ±3 and ±9 T fields for 2 min. Followed by that, magnetic field sweeps between ± 0.2 T were then performed. As shown in **Figure 4**a, in all Al-Cr_2O_3 initialization scenarios, a pronounced exchange bias was observed, and overlapping hysteresis loops were obtained. This observation indicates that field training and field cooling are equally effective methods for initializing the magnetism in Al-Cr_2O_3 and consequently establishing exchange bias in this system.

The exchange bias is also shown to be directly related to Al-Cr_2O_3 magnetization from the continuous dependence of exchange bias on the externally applied training field. Before each field sweep (±0.2 T), a negative exchange bias was set using a +3 T field, and then the sample was subsequently subjected to a training field of opposing sign $-\mu_0 H_{train}$ (Figure 4b). The magnitude of this training field was increased from 0.2 to 3 T, resulting in a gradual switching of Al-Cr_2O_3 magnetization and more granular control of the exchange bias. As shown in Figure 4b, the anomalous Hall loop of CBST gradually shifts to the positive direction, through a sign change in the exchange bias, and finally saturates with increasing training field. In this measurement series, zero exchange bias occurs at a training field of 0.7 T, and the exchange bias magnitude saturates at ≈1 T. These values match the coercivity and switching fields of Al-Cr_2O_3 obtained from the SQUID data in Figure 1b, indicating the exchange bias in CBST is directly correlated to Al-Cr_2O_3 magnetization, and is in excellent agreement with prior studies.[26] The same measurement was performed at different temperatures, and the exchange bias as a function of training field magnitude was obtained and shown in the color plot in Figure 4c. The inset schematically illustrates the different signs of exchange bias under different training fields due to the antiparallel alignment of the CBST and Al-Cr_2O_3 surface spins. The temperature dependence of $|H_{eb}|$ is summarized in Figure 4d, where the exchange bias magnitude decreases with increasing temperature and vanishes when the temperature reaches above the Curie temperature (≈25 K) of CBST thin film. This observation, combined with the absence of magnetic proximity effects in an undoped BST and Al-Cr_2O_3 heterostructure (Figure S4, Supporting Information), indicates the exchange coupling of Cr atoms between Al-Cr_2O_3 and CBST plays an important role in the exchange bias.

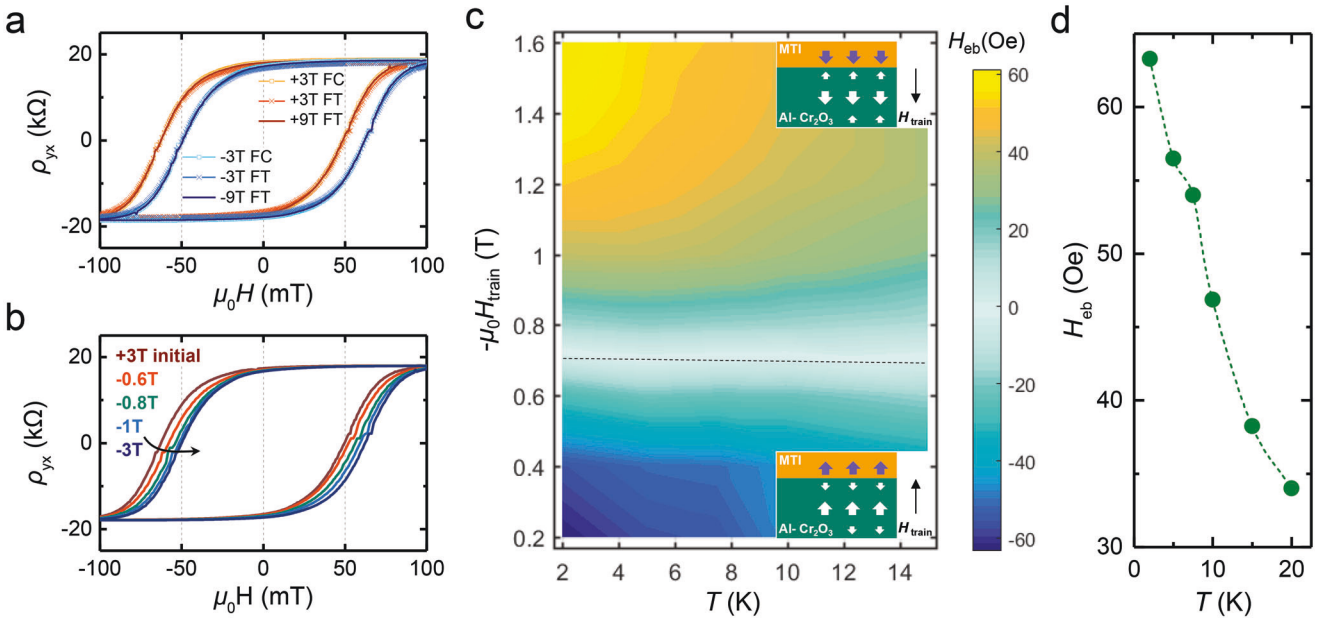

Figure 4. Exchange bias manipulated by field-training of Al-Cr_2O_3. a) Small field sweep (±0.2 T) of ρ_{yx} at $T = 2$ K, after treating the sample with ±3 T, ±9 T field training (FT) and ±3 T field-cooling (FC) processes. b) Small field sweep (±0.2 T) of ρ_{yx} at $T = 2$ K, after sample treated with various training field. +3 T field is applied to initialize the magnetization of Al-Cr_2O_3 before each field-training and loop scan. c) Mapping of the training field dependent exchange bias H_{eb} at different temperatures. The gradual switching of H_{eb} with increasing training field corresponds to the switching of the Al-Cr_2O_3 magnetization. d) Summarized temperature dependence of H_{eb}. The same device that has been described in Figure 3 is studied for this measurement.

3. Conclusion

To summarize, we demonstrate high quality MBE growth of CBST on an uncompensated AFM insulator substrate (Al-Cr_2O_3). PNR measurements reveal a vanishing in-plane magnetization at the Al-Cr_2O_3 and CBST interface, which, when taken together with the transport measurements, indicates a strong exchange coupling between the two magnetic layers pinning the moments at the interface to point out-of-plane. Thanks to the parasitic magnetization, Al-Cr_2O_3 hosts several advantages over pristine Cr_2O_3 such as enabling reliable realization of a single domain state in the AFM layer. While prior achievements of exchange bias in undoped Cr_2O_3/MTI heterostructures never coincided with quantized behavior, the exchange bias and the QAH effect were observed simultaneously for the first time in Al-Cr_2O_3/CBST. This exchange biased QAH effect could potentially facilitate the development of functional topological spintronic devices when taking advantages of the magnetoelectric effect of Al-Cr_2O_3.[35,36] We further demonstrate that the magnitude and sign of the exchange bias can be effectively and reproducibly controlled by a novel field training process to set the magnetization of the Al-Cr_2O_3 layer. This magnetic controllability eliminates the impractically slow and energy inefficient requirement of thermal training the AFM to control the exchange bias in the bilayer system. This work successfully demonstrates the manipulation of QAH states by an adjacent magnetic layer through exchange coupling, which provides an additional degree of freedom through which the topological surface states can be manipulated. Our findings highlight the rich tuning possibilities in topological and AFM heterostructures, and demonstrate heretofore unrealized capabilities in MTI exchange bias engineering. This approach can also be used to understand and manipulate other emerging topological quantum phases such as axion insulator states[41–43] and high-Chern number QAH states.[44]

4. Experimental Section

MBE Growth and Sample Characterizations: The single crystal Al-doped Cr_2O_3 (50 nm) thin films were grown on Al_2O_3 (0001) substrate using the reactive sputtering method in an Ar + O_2 atmosphere at a substrate temperature of 773 K with a Al_5Cr_{95} alloy target.[35,36] The Al-doped Cr_2O_3 films were then transferred through air, and high-quality Cr-doped $Bi_xSb_{2-x}Te_3$ thin films were grown using a Perkin Elmer MBE system in ultrahigh vacuum. High-purity Bi (99.9999%), Te (99.9999%), Cr (99.99%), and Sb (99.999%) were evaporated by conventional effusion cells and cracker cells. During the growth, the substrate was maintained at a temperature of 200 °C. The growth was monitored by an in-situ reflection high-energy electron diffraction (RHEED). The SQUID characterization was done in a Quantum Design Magnetic Properties Measurement System (MPMS3). SQUID data were presented with linear background associated with the substrate's diamagnetic signature subtracted.

Device Fabrication and Transport Measurement: Grown films were patterned into Hall bars for the transport study using a hard mask with dry etching methods. Low-frequency four-probe magnetoresistance measurements and Hall measurements were conducted in a Quantum Design Physical Properties Measurement System (PPMS) with a dilution refrigerator insert.

Polarized Neutron Reflectometry (PNR) Measurements: Polarized neutron reflectometry (PNR) measurements were performed with the Polarized Beam Reflectometer (PBR) instrument at the NIST Center for Neutron Research. Samples were field-cooled, in an applied field of 3 T in-plane, to a temperature of 6 K; spin-up and spin-down non-spin-flip reflectivities (R^{++} and R^{--}) were then measured in a specular configuration at in-plane fields of 3 T, 250 mT, and 110 mT. Data was reduced as the sum and difference

of these cross-sections using the Reductus software package, and then fit simultaneously using Refl1d to model the nuclear and magnetic scattering length densities (SLD) as a function of depth within the sample; further details can be found in the section S2 (Supporting Information).

Statistical Analysis: PNR data was reduced as the sum and difference of the non-spin-flip cross-sections ($R^{++}+R^{--}$ and $R^{++}-R^{--}$) using the Reductus software package.[45] Incident beam intensity was corrected for as a function of angle (beam footprint on the sample) and polarization optics, using direct beam measurements for each polarization configuration. Background detector signal, measured at an angle of 1° from the reflection, was subtracted. The data from all field conditions were then fit simultaneously using Refl1d[46] to model the nuclear and magnetic scattering length densities (SLD) as a function of depth within the sample. In this software, a slab model was constructed, allowing layer thickness, nuclear SLD, roughness, and magnetization of each slab to vary. The reflectivity for an incident spin-polarized neutron of wavevector Q from this scattering potential was calculated, and the parameters adjusted to minimize χ^2 between the data and simulated R(Q) using a population-based algorithm. Parameter uncertainties were calculated using Bayesian analysis implemented in the DREAM Markov Chain Monte Carlo method of Bumps.[47] Further details and model selection can be found in the section S2 (Supporting Information). All quoted uncertainties and error bars represent ±1 standard deviation (68% confidence interval). Data is presented as mean(std) where the number in parentheses is the uncertainty on the corresponding last digits of the quoted result.

Supporting Information

Supporting Information is available from the Wiley Online Library or from the author.

Acknowledgements

This work was supported by the NSF under Grants no. 1936383 and no. 2040737, the U.S. Army Research Office MURI program under Grants no. W911NF-20-2-0166 and no. W911NF-16-1-0472. C.E. is an employee of Fibertek, Inc. and performs in support of Contract no. W15P7T19D0038, Delivery Order W911-QX-20-F-0023. The views expressed are those of the authors and do not reflect the official policy or position of the Department of Defense or the US government. The identification of any commercial product or tradename does not imply endorsement or recommendation by Fibertek Inc. T.N. and M.S. were funded by the ImPACT Program of Council for Science, Technology, and Innovation (Cabinet Office, Japan Government). E.E. and N.N. were supported by the U.S. Department of Energy (DOE), Office of Science, Office of Basic Energy Sciences under Award no. DE-SC0021117. The research was performed in part at the National Institute of Standards and Technology (NIST). Any mention of specific trade names and commercial products is for information and experimental reproducibility only; it does not imply recommendation or endorsement by NIST.

Conflict of Interest

The authors declare no conflict of interest.

Author Contributions

P.Z. and P.P.B. contributed equally to this work. P.Z. and K.L.W. conceived and designed the research. P.Z., L.P., T.N., and M.S. performed the sample growth. M.E.H. performed the TEM characterization. C.E. performed the SQUID measurements. S.C. fabricated the device. P.Z. and P.D. performed transport measurements with the help of E.E. and N.N.P.Z. analyzed the transport data. P.P.B., P.Q., B.B.M., and A.G. performed the PNR measurement and data analysis. G.Q. contributed to data collection of some additional experiments which were conducted for the revision. P.Z., P.P.B., A.G., and K.L.W. wrote the manuscript with the inputs from all the other co-authors.

Data Availability Statement

The data that support the findings of this study are available on request from the corresponding author. The data are not publicly available due to privacy or ethical restrictions.

Keywords

antiferromagnet, exchange bias, quantum anomalous Hall, topological insulators

Received: January 13, 2023
Revised: February 28, 2023
Published online: June 27, 2023

[1] C. Z. Chang, J. Zhang, X. Feng, J. Shen, Z. Zhang, M. Guo, K. Li, Y. Ou, P. Wei, L.-L. Wang, Z.-Q. Ji, Y. Feng, S. Ji, X. Chen, J. Jia, X. Dai, Z. Fang, S.-C. Zhang, K. He, Y. Wang, L. Lu, X.-C. Ma, Q.-K. Xue, *Science* **2013**, *340*, 167.
[2] X. Kou, S.-T. Guo, Y. Fan, L. Pan, M. Lang, Y. Jiang, Q. Shao, T. Nie, K. Murata, J. Tang, Y. Wang, L. He, T.-K. Lee, W.-L. Lee, K. L. Wang, *Phys. Rev. Lett.* **2014**, *113*, 137201.
[3] X. Kou, L. Pan, J. Wang, Y. Fan, E. S. Choi, W.-L. Lee, T. Nie, K. Murata, Q. Shao, S.-C. Zhang, K. L. Wang, *Nat. Commun.* **2015**, *6*, 8474.
[4] J. G. Checkelsky, R. Yoshimi, A. Tsukazaki, K. S. Takahashi, Y. Kozuka, J. Falson, M. Kawasaki, Y. Tokura, *Nat. Phys.* **2014**, *10*, 731.
[5] M. Mogi, R. Yoshimi, A. Tsukazaki, K. Yasuda, Y. Kozuka, K. S. Takahashi, M. Kawasaki, Y. Tokura, *Appl. Phys. Lett.* **2015**, *107*, 182401 .
[6] C.-Z. Chang, W. Zhao, D. Y. Kim, H. Zhang, B. A. Assaf, D. Heiman, S.-C. Zhang, C. Liu, M. H. W. Chan, J. S. Moodera, *Nat. Mater.* **2015**, *14*, 473.
[7] Y. Deng, Y. Yu, M. Z. Shi, Z. Guo, Z. Xu, J. Wang, X. H. Chen, Y. Zhang, *Science* **2020**, *367*, 895.
[8] M. Serlin, C. L. Tschirhart, H. Polshyn, Y. Zhang, J. Zhu, K. Watanabe, T. Taniguchi, L. Balents, A. F. Young, *Science* **2020**, *367*, 900.
[9] T. Li, S. Jiang, B. Shen, Y. Zhang, L. Li, Z. Tao, T. Devakul, K. Watanabe, T. Taniguchi, L. Fu, J. Shan, K. F. Mak, *Nature* **2021**, *600*, 641.
[10] M. Lang, M. Montazeri, M. C. Onbasli, X. Kou, Y. Fan, P. Upadhyaya, K. Yao, F. Liu, Y. Jiang, W. Jiang, K. L. Wong, G. Yu, J. Tang, T. Nie, L. He, R. N. Schwartz, Y. Wang, C. A. Ross, K. L. Wang, *Nano Lett.* **2014**, *14*, 3459.
[11] X. Che, K. Murata, L. Pan, Q. L. He, G. Yu, Q. Shao, G. Yin, P. Deng, Y. Fan, B. Ma, X. Liang, B. Zhang, X. Han, L. Bi, Q.-H. Yang, H. Zhang, K. L. Wang, *ACS Nano* **2018**, *12*, 5042.
[12] Z. Jiang, C.-Z. Chang, C. Tang, P. Wei, J. S. Moodera, J. Shi, *Nano Lett.* **2015**, *15*, 5835.
[13] C. Tang, C. Z. Chang, G. J. Zhao, Y. W. Liu, Z. L. Jiang, C. X. Liu, M. R. McCartney, D. J. Smith, T. Y. Chen, J. S. Moodera, J. Shi, *Sci. Adv.* **2017**, *3*, e1700307.
[14] P. Wei, F. Katmis, B. A. Assaf, H. Steinberg, P. Jarillo-Herrero, D. Heiman, J. S. Moodera, *Phys. Rev. Lett.* **2013**, *110*, 186807.
[15] F. Katmis, V. Lauter, F. S. Nogueira, B. A. Assaf, M. E. Jamer, P. Wei, B. Satpati, J. W. Freeland, I. Eremin, D. Heiman, P. Jarillo-Herrero, J. S. Moodera, *Nature* **2016**, *533*, 513.
[16] C. Lee, F. Katmis, P. Jarillo-Herrero, J. S. Moodera, N. Gedik, *Nat. Commun.* **2016**, *7*, 12014.
[17] L. D. Alegria, H. Ji, N. Yao, J. J. Clarke, R. J. Cava, J. R. Petta, *Appl. Phys. Lett.* **2014**, *105*, 053512.
[18] R. Watanabe, R. Yoshimi, M. Kawamura, M. Mogi, A. Tsukazaki, X. Z. Yu, K. Nakajima, K. S. Takahashi, M. Kawasaki, Y. Tokura, *Appl. Phys. Lett.* **2019**, *115*, 102403.

[19] M. Mogi, T. Nakajima, V. Ukleev, A. Tsukazaki, R. Yoshimi, M. Kawamura, K. S. Takahashi, T. Hanashima, K. Kakurai, T.-H. Arima, M. Kawasaki, Y. Tokura, *Phys. Rev. Lett.* **2019**, *123*, 016804.
[20] W. Liu, L. He, Y. Xu, K. Murata, M. C. Onbasli, M. Lang, N. J. Maltby, S. Li, X. Wang, C. A. Ross, P. Bencok, G. Van Der Laan, R. Zhang, K. L. Wang, *Nano Lett.* **2015**, *15*, 764.
[21] M. Li, C.-Z. Chang, B. J. Kirby, M. E. Jamer, W. Cui, L. Wu, P. Wei, Y. Zhu, D. Heiman, J. Li, J. S. Moodera, *Phys. Rev. Lett.* **2015**, *115*, 087201.
[22] Q. L. He, X. Kou, A. J. Grutter, G. Yin, L. Pan, X. Che, Y. Liu, T. Nie, B. Zhang, S. M. Disseler, B. J. Kirby, W. Ratcliff Ii, Q. Shao, K. Murata, X. Zhu, G. Yu, Y. Fan, M. Montazeri, X. Han, J. A. Borchers, K. L. Wang, *Nat. Mater.* **2017**, *16*, 94.
[23] C.-Y. Yang, L. Pan, A. J. Grutter, H. Wang, X. Che, Q. L. He, Y. Wu, D. A. Gilbert, P. Shafer, E. Arenholz, H. Wu, G. Yin, P. Deng, J. A. Borchers, W. Ratcliff, K. L. Wang, *Sci. Adv.* **2020**, *6*, eaaz8463.
[24] L. Pan, A. Grutter, P. Zhang, X. Che, T. Nozaki, A. Stern, M. Street, B. Zhang, B. Casas, Q. L. He, E. S. Choi, S. M. Disseler, D. A. Gilbert, G. Yin, Q. Shao, P. Deng, Y. Wu, X. Liu, X. Kou, S. Masashi, X. Han, C. Binek, S. Chambers, J. Xia, K. L. Wang, *Adv. Mater.* **2020**, *32*, 2001460.
[25] J. Liu, A. Singh, Y. Y. F. Liu, A. Ionescu, B. Kuerbanjiang, C. H. W. Barnes, T. Hesjedal, *Nano Lett.* **2020**, *20*, 5315.
[26] F. Wang, D. Xiao, W. Yuan, J. Jiang, Y.-F. Zhao, L. Zhang, Y. Yao, W. Liu, Z. Zhang, C. Liu, J. Shi, W. Han, M. H. W. Chan, N. Samarth, C.-Z. Chang, *Nano Lett.* **2019**, *19*, 2945.
[27] Q. L. He, G. Yin, A. J. Grutter, L. Pan, X. Che, G. Yu, D. A. Gilbert, S. M. Disseler, Y. Liu, P. Shafer, B. Zhang, Y. Wu, B. J. Kirby, E. Arenholz, R. K. Lake, X. Han, K. L. Wang, *Nat. Commun.* **2018**, *9*, 2767.
[28] S. Grauer, S. Schreyeck, M. Winnerlein, K. Brunner, C. Gould, L. W. Molenkamp, *Phys. Rev. B* **2015**, *92*, 201304.
[29] E. O. Lachman, A. F. Young, A. Richardella, J. Cuppens, H. R. Naren, Y. Anahory, A. Y. Meltzer, A. Kandala, S. Kempinger, Y. Myasoedov, M. E. Huber, N. Samarth, E. Zeldov, *Sci. Adv.* **2015**, *1*, e1500740.
[30] I. Lee, C. K. Kim, J. Lee, S. J. L. Billinge, R. Zhong, J. A. Schneeloch, T. Liu, T. Valla, J. M. Tranquada, G. Gu, J. C. S. Davis, *Proc. Natl. Acad. Sci. USA* **2015**, *112*, 1316.
[31] T. Ashida, M. Oida, N. Shimomura, T. Nozaki, T. Shibata, M. Sahashi, *Appl. Phys. Lett.* **2014**, *104*, 152409.
[32] T. Ashida, M. Oida, N. Shimomura, T. Nozaki, T. Shibata, M. Sahashi, *Appl. Phys. Lett.* **2015**, *106*, 132407.
[33] X. He, Y. Wang, N. Wu, A. N. Caruso, E. Vescovo, K. D. Belashchenko, P. A. Dowben, C. Binek, *Nat. Mater.* **2010**, *9*, 579.
[34] W. Echtenkamp, C. Binek, *Phys. Rev. Lett.* **2013**, *111*, 187204.
[35] T. Nozaki, M. Al-Mahdawi, Y. Shiokawa, S. P. Pati, S. Ye, Y. Kotani, K. Toyoki, T. Nakamura, M. Suzuki, S. Yonemura, T. Shibata, M. Sahashi, *Phys Status Solidi Rapid Res Lett* **2018**, *12*, 1800366.
[36] T. Nozaki, M. Al-Mahdawi, Y. Shiokawa, S. P. Pati, H. Imamura, M. Sahashi, *J. Appl. Phys.* **2020**, *128*, 023901.
[37] L. J. Riddiford, A. J. Grutter, T. Pillsbury, M. Stanley, D. Reifsnyder Hickey, P. Li, N. Alem, N. Samarth, Y. Suzuki, *Phys. Rev. Lett.* **2022**, *128*, 126802.
[38] Y. Lv, J. Kally, T. Liu, P. Quarterman, T. Pillsbury, B. J. Kirby, A. J. Grutter, P. Sahu, J. A. Borchers, M. Wu, N. Samarth, J.-P. Wang, *Appl. Phys. Rev.* **2022**, *9*, 011406.
[39] J. Wang, B. Lian, S.-C. Zhang, *Phys. Rev. B* **2014**, *89*, 085106.
[40] Y. Feng, X. Feng, Y. Ou, J. Wang, C. Liu, L. Zhang, D. Zhao, G. Jiang, S.-C. Zhang, K. He, X. Ma, Q.-K. Xue, Y. Wang, *Phys. Rev. Lett.* **2015**, *115*, 126801.
[41] M. Mogi, M. Kawamura, A. Tsukazaki, R. Yoshimi, K. S. Takahashi, M. Kawasaki, Y. Tokura, *Sci. Adv.* **2017**, *3*, eaao1669.
[42] M. Mogi, M. Kawamura, R. Yoshimi, A. Tsukazaki, Y. Kozuka, N. Shirakawa, K. S. Takahashi, M. Kawasaki, Y. Tokura, *Nat. Mater.* **2017**, *16*, 516.
[43] D. Xiao, J. Jiang, J.-H. Shin, W. Wang, F. Wang, Y.-F. Zhao, C. Liu, W. Wu, M. H. W. Chan, N. Samarth, C.-Z. Chang, *Phys. Rev. Lett.* **2018**, *120*, 056801.
[44] Y.-F. Zhao, R. Zhang, R. Mei, L.-J. Zhou, H. Yi, Y.-Q. Zhang, J. Yu, R. Xiao, K. Wang, N. Samarth, M. H. W. Chan, C.-X. Liu, C.-Z. Chang, *Nature* **2020**, *588*, 419.
[45] B. Maranville, W. Ratcliff Ii, P. Kienzle, *J. Appl. Crystallogr.* **2018**, *51*, 1500.
[46] P. A. Kienzle, Refl1D [Computer Software], https://github.com/reflectometry/refl1d/tree/change-of-basis (accessed: February 2023).
[47] P. A. Kienzle, J. Krycka, N. Patel, I. Sahin, "Bumps [Computer Software]. College Park, MD: University of Maryland.," **2011**.